ACS APPLIED MATERIALS & INTERFACES

Research Article

Cite This: ACS Appl. Mater. Interfaces 2019, 11, 44444−44450

www.acsami.org

# Morphology Evolution during Lithium-Based Vertically Aligned Nanocomposite Growth

Daniel M. Cunha, Chris M. Vos, Theodoor A. Hendriks, Deepak P. Singh, and Mark Huijben*

MESA+ Institute for Nanotechnology, University of Twente, 7500 AE Enschede, Overijssel, Netherlands

**ABSTRACT:** Ceramic-based nanocomposites are a rapidly evolving research area as they are currently being used in a wide range of applications. Epitaxial vertically aligned nanocomposites (VANs) offer promising advantages over conventional planar multilayers as key functionalities are tailored by the strong coupling at their vertical interfaces. However, limited knowledge exists of which material systems are compatible in composite films and which types of structures are optimal for a given functionality. No lithium-based VANs have yet been explored for energy storage, while 3D solid-state batteries offer great promise for enhanced energy and power densities. Although solid-on-solid kinetic Monte Carlo simulation (KMCS) models of VAN growth have previously been developed, phase separation was forced into the systems by limiting hopping directions and/or tuning the activation energies for hopping. Here, we study the influence of the temperature and deposition rate on the morphology evolution of lithium-based VANs, consisting of a promising $LiMn_2O_4$ cathode and a $Li_{0.5}La_{0.5}TiO_3$ electrolyte, by applying a KMCS model with activation energies for hopping obtained experimentally and with minimum restrictions for hopping directions. Although the model considers only the kinetic processes away from thermodynamic equilibrium, which would determine the final shape of the pillars within the matrix, the trends in pillar size and distribution within the simulated VANs are in good agreement with experiments. This provides an elegant tool to predict the growth of VAN materials as the experimental activation energies and higher degrees of freedom for hopping result in a more realistic and low computational cost model to obtain accurate simulations of VAN materials.

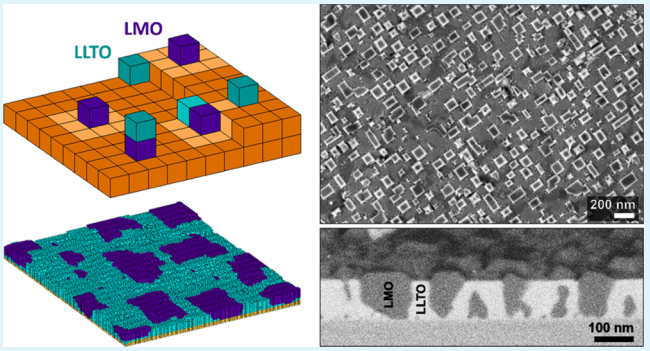


**KEYWORDS:** *nanocomposites, lithium battery, self-assembly, kinetic Monte Carlo simulation, pulsed laser deposition*

## INTRODUCTION

Nanocomposites have attracted great interest over the last decades due to the presence of enhanced functional material properties induced by confinement of the structural dimensions.[1] Ceramic-based nanocomposites are one of the most rapidly evolving research areas[2] as they are currently being used in a wide range of applications, such as motor engines, heat exchangers, power plants, and air-/spacecraft technology. However, accurate control of the distribution and orientation of the nanoparticles within the matrix material is often limited or even impossible. Detailed knowledge on the alignment of nanostructures through self-assembly is very well-studied in organic systems[3] but remains a rather unexplored territory for inorganic nanocomposites.

Parallel to planar heterointerfaces, vertical heteroepitaxial nanocomposite thin films have been developed in the past decade as a new platform for creating self-assembled device architectures and multifunctionalities.[4,5] Such epitaxial vertically aligned nanocomposites (VANs) offer promising advantages over conventional planar multilayers as key functionalities are tailored by the strong coupling between the two phases at their interfaces, such as strain-enhanced ferroelectricity and multiferroics,[6,7] ferromagnetism,[8] magneto-resistance,[9] electronic transport,[10] and coupled dielectric and optical effects.[11]

Epitaxial VANs are self-assembled through physical vapor deposition, without control of the deposition sequence, as is required for planar multilayer films. For epitaxially directed self-assembly, it is desirable that one phase in the film is structurally well-matched to the substrate such that it nucleates, grows epitaxially, and forms the host matrix. The second phase (epiphyte) epitaxially aligns with the matrix phase. Depending on surface energy considerations and the relative concentrations of the two components in the film, the epiphyte phase may or may not seed its growth on the substrate. The host and epiphyte can both be chosen to be active phases whose functional properties are of interest and where the phases interact with each other via strain- or charge-coupling at the interfaces. Dimensional tunability has been demonstrated, in which various nanopillar shapes and dimensions (2−200 nm) have been achieved in specific material systems.[4,5]

Received: August 21, 2019
Accepted: November 5, 2019
Published: November 5, 2019






DOI: 10.1021/acsami.9b15025
ACS Appl. Mater. Interfaces 2019, 11, 44444−44450

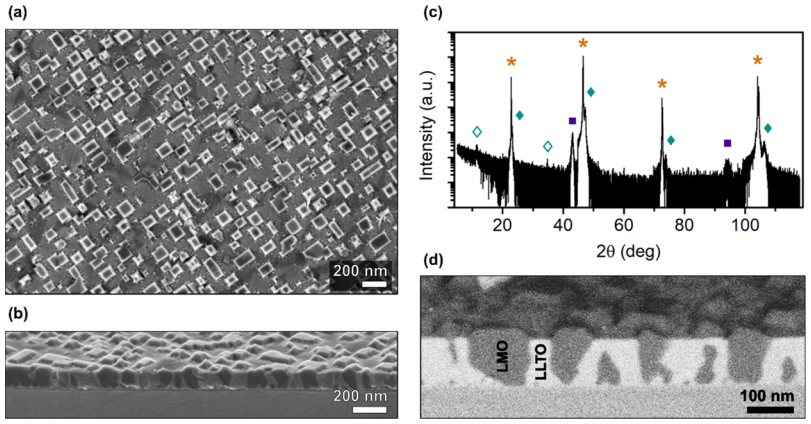


**Figure 1.** (a) Top-view and (b) cross-sectional SEM images of a nanocomposite thin film composed of LMO pillars embedded in an LLTO matrix. (c) X-ray diffraction analysis of the VAN film, in which LLTO peaks are shown by ◆, LMO peaks by ■, and STO substrate peaks by *, whereas minor contributions of the tetragonal LLTO phase are indicated by ◇. (d) Cross-sectional energy selective backscattered scanning electron microscopy (SEM) image showing the compositional contrast.

There is currently limited knowledge of which materials systems are compatible with one another in composite films and which types of structures are optimal for a given functionality.[12] In order to be able to design optimal VAN structures, the current knowledge gap on the fundamental understanding of the growth mechanisms during composite nanostructure formation must be filled. Detailed simulation of the VAN growth mechanism would provide important insight into the compositional, structural, and processing factors that influence the achievable VAN structures. Solid-on-solid kinetic Monte Carlo simulation (KMCS) models of vertical nanocomposite growth have previously been developed to study the influence of temperature,[13−16] deposition rate,[14,17] and composition ratio[13,15] on the VAN morphology. Although the studied models result in good approximation of the experimental results, they force phase separation into the nanocomposite system[13−17] by limiting the permitted hopping orientations and/or by tuning the activation energies for hopping to fit the experimental results.

Although various epitaxial VANs have been studied in the last decade,[4,5] the successful realization of two-phase epitaxial VANs has remained limited to specific material combinations: for example, ferroelectrics ($BaTiO_3$, $BiFeO_3$, and $PbTiO_3$) with ferromagnets ($CoFe_2O_4$, $NiFe_2O_4$, $MgFe_2O_4$, $La_{0.7}Sr_{0.3}MnO_3$, and $Fe_3O_4$); $BiFeO_3$ ferroelectric with $LaFeO_3$ antiferromagnets; and a ZnO insulator with a $La_{0.7}Sr_{0.3}MnO_3$ ferromagnet. No lithium-based VANs have yet been explored for energy storage, while 3D solid-state batteries offer great promise for enhanced energy and power densities.[18,19] The potential advantages of VAN-based lithium-ion batteries are a larger electrode/electrolyte contact area leading to higher (dis)charge rates; short path lengths for both electronic and Li-ion transport leading to a higher lithium-ion flux (also permitting the usage of materials with low electronic or ionic conductivity); better accommodation of the strain during lithium insertion/extraction; and interface reactions not available in bulk materials.

Here, we study the influence of the temperature and deposition rate on the morphology evolution of lithium-based VANs by applying a KMCS model with activation energies for hopping obtained experimentally and with minimum restrictions for hopping directions. The combination of KMCS and reflective high energy electron diffraction (RHEED) measurements provides an elegant tool to predict the growth of VAN materials. Although the model considers only the kinetic processes away from thermodynamic equilibrium, which would determine the final shape of the pillars within the matrix, the trends in pillar size and distribution within the simulated VANs are in good agreement with experiments. We demonstrate that experimental activation energies and higher degrees of freedom for hopping result in a more realistic and low computational cost model that can be used to obtain accurate simulation results for VAN materials. Furthermore, we demonstrate the successful growth of lithium-based VANs consisting of the promising $LiMn_2O_4$ cathode and $Li_{0.5}La_{0.5}TiO_3$ electrolyte materials.

## RESULTS AND DISCUSSION

For the proposed KMCS algorithm, we model the VAN growth of $LiMn_2O_4$ (LMO) pillars embedded in a $Li_{0.5}La_{0.5}TiO_3$ (LLTO) matrix, deposited on a (100)-oriented $SrTiO_3$ (STO) substrate, as displayed in Figure 1a,b, to have a better understanding of the influence of growth parameters on the VAN formation.

LMO is a high voltage cathode material[20] exhibiting a spinel structure with a lattice parameter of $a$ = 8.245 Å, while LLTO is a high ionic conducting electrolyte[21] with a perovskite structure ($a$ = 3.904 Å), making them an interesting combination, similar to previous successful spinel−perovskite VAN formations.[6,22] The successful phase separation of both materials into a nanopillar matrix structure within the nanocomposite can be observed in the SEM images, as shown in Figure 1a,b, while the purity and crystallinity of both specific phases are confirmed by X-ray diffraction (XRD), Figure 1c. The out-of-plane (100) crystal orientations of both LMO and LLTO phases within the VAN films are aligned with the orientation of the STO substrate. The LMO and LLTO peaks show the presence of highly crystalline oriented spinel and perovskite structures, in good agreement with previous studies of individual LMO or LLTO thin films grown on STO(100) substrates.[23,24] The small extra peaks suggest the presence of minor contributions of tetragonal LLTO ($Li_{0.56}La_{0.33}TiO_3$), which could be randomly distributed throughout the LLTO matrix or located at specific interfaces. This minority tetragonal LLTO phase will be studied in detail in follow-up research. Also, the in-plane orientations of both


DOI: 10.1021/acsami.9b15025
ACS Appl. Mater. Interfaces 2019, 11, 44444−44450

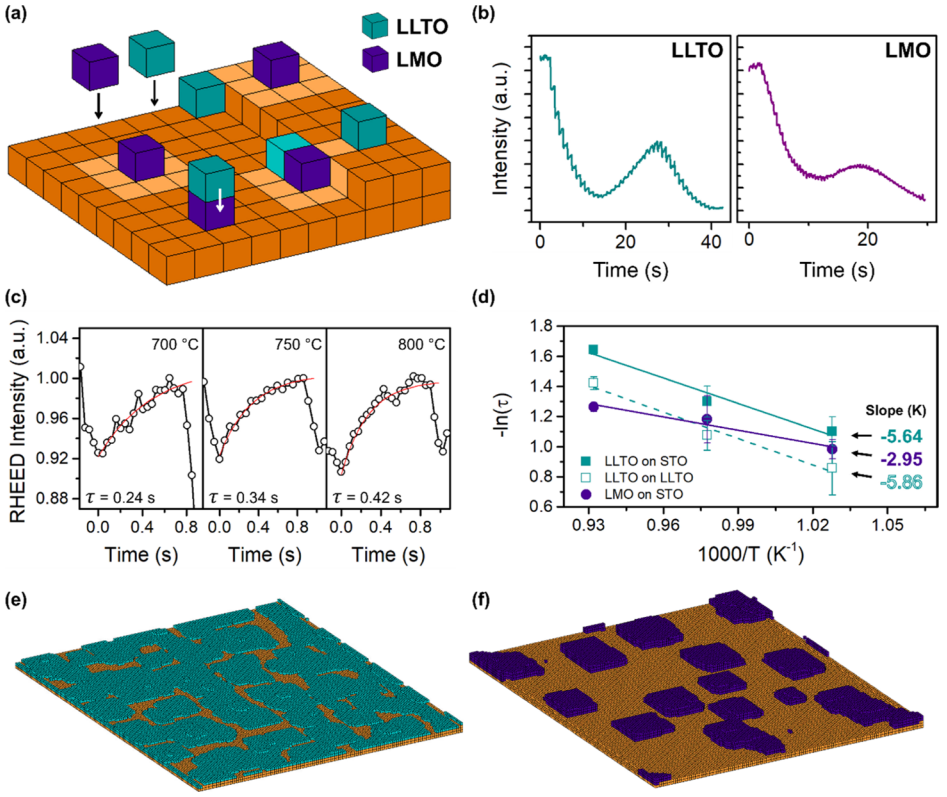


**Figure 2.** (a) Schematic of the KMCS model, representing the deposition and diffusion of both phases, LMO (purple) and LLTO (green), on a STO (orange) surface. The bright areas indicate possible hopping positions for LMO adatoms on the surface. Note that adatoms that could lead to floating adatoms (indicated by the white arrow) have no possible hopping direction. (b) RHEED intensity oscillations during PLD growth of individual LLTO and LMO thin films on STO substrates. (c) Exponential fitting of the specular spot RHEED intensity variation during a single laser pulse for LLTO growth on the LLTO surface at different temperatures. (d) Arrhenius plot of the RHEED relaxation time dependence on the growth temperatures for several combinations: LLTO on STO, LLTO on LLTO, and LMO on STO. (e,f) KMC simulation showing the wetting and nonwetting behavior of LLTO and LMO thin films on a STO surface based on 12 deposition pulses using the activation energies for hopping as obtained by RHEED analysis.

**Table 1. Activation Energies Obtained by RHEED (in eV) and Constants Used in the KMCS Model**

| $k_0$ | $E_S$ | $E_{ES}$ | $E_{LMO-STO}$ | $E_{LMO-LMO}$ | $E_{LLTO-LMO}$ | $E_{LLTO-STO}$ | $E_{LLTO-LLTO}$ |
|---|---|---|---|---|---|---|---|
| $10^{12}$ | 1.0 | 0.15 | 0.25 ± 0.01 | 0.51 ± 0.01 | 0.25 ± 0.01 | 0.49 ± 0.01 | 0.51 ± 0.01 |

cubic LMO and LLTO phases are aligned to the cubic substrate as confirmed by detailed XRD analysis (not shown), resulting in square LMO nanopillars rotated 45° with respect to the (010) in-plane direction of both the perovskite LLTO matrix and STO substrate. Furthermore, phase separation was also confirmed by energy selective backscattered SEM analysis, where contrast is determined by compositional differences (Figure 1d), leading to a much brighter LLTO matrix because of the presence of the heavy La ions.

The KMCS modeling is represented in Figure 2a, where a 3-dimensional 128 × 128 × $Z$ grid is used to represent the cubic (100) surface of STO. For each pulse, atoms are generated on random locations of the grid, and one adatom represents one unit cell of the LLTO perovskite crystal structure or 1/8th unit cell of the LMO spinel crystal structure. After each pulse, the deposited adatoms diffuse over the surface, one at a time. Periodic boundary conditions were used, and hopping can occur in the 6 cubic and 12 diagonal directions, only if a site is unoccupied and there is a path available to it, indicated by the highlighted positions in Figure 2a. The LMO (purple, indicated by the white arrow) adatom in Figure 2a represents an adatom with a hopping rate of zero because its movement would cause a floating adatom. To obtain the accurate activation energies for hopping for all involved materials, a systematic RHEED study was performed during thin-film growth. With three different materials, there are five possible interaction energies: $E_{LMO-STO}$, $E_{LMO-LMO}$, $E_{LLTO-LMO}$, $E_{LLTO-STO}$, and $E_{LLTO-LLTO}$. More details about the algorithm employed in the KMCS model are given in the Method Section.

Typical RHEED measurements are shown in Figure 2b, where individual LLTO and LMO thin films were deposited on (100)-oriented STO substrates. The activation energies for hopping were extracted by monitoring the recovery of the specular spot RHEED intensity for laser pulses at growth temperatures of 700, 750, and 800 °C. The relaxation curves are fitted to an exponential function (Figure 2c), given by $I \propto I_0(1 - e^{-t/\tau})$,[25] and the time constant obtained is a measure of the mobility of the diffusing adatoms with $\ln(\tau) = A + B \cdot 1/T$, where $A = \ln(l_D^2/\nu a^2)$, $B = E_A/k_B$, $l_D$ is the diffusion length, $\nu$ is the diffusion attempt frequency, and $a$ is the characteristic jump distance. Therefore, using the obtained relaxation time $\tau$, an Arrhenius plot can be drawn (Figure 2d), where the slope is used to calculate the activation energy $E_A$ for each materials


DOI: 10.1021/acsami.9b15025
ACS Appl. Mater. Interfaces 2019, 11, 44444−44450

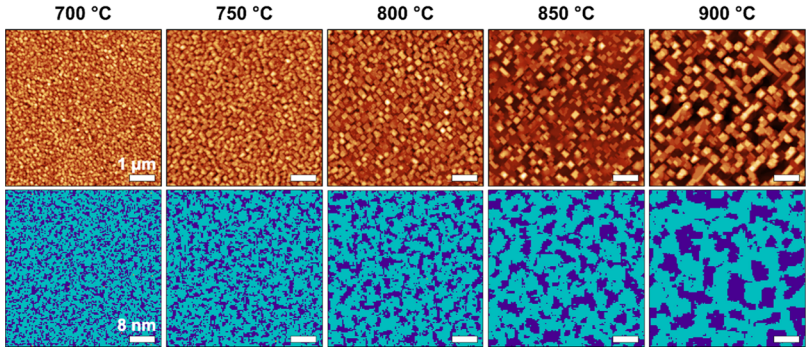


**Figure 3.** AFM images (top) and KMCS results (bottom) for the LMO−LLTO nanocomposite growth at a deposition rate of 20 Hz for different growth temperatures.

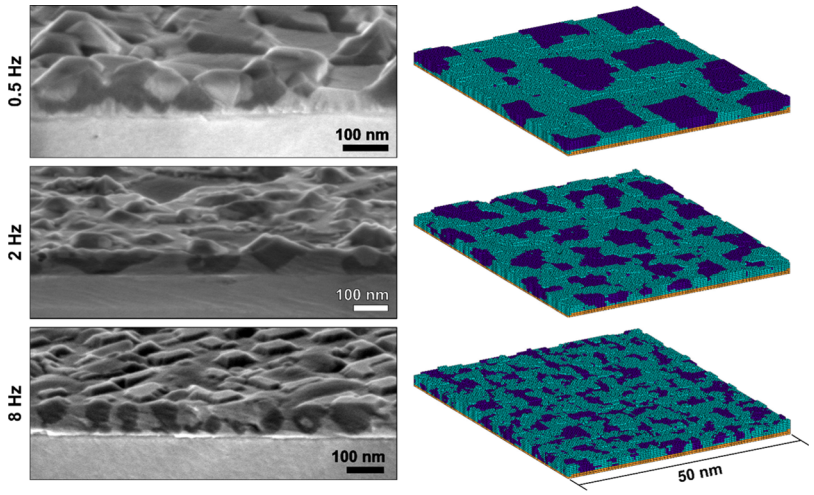


**Figure 4.** Cross-sectional SEM analysis (left) and 3D view of KMCS results (right) for the LMO−LLTO nanocomposite growth for different deposition rates (0.5, 2, and 8 Hz) at 800 °C.

combination.[26] From the initial growth of the first LLTO or LMO layer on a STO surface, the $E_{LLTO-STO}$ and $E_{LMO-STO}$ interaction energies were determined, while subsequent thin-film growth resulted in values for $E_{LLTO-LLTO}$ and $E_{LMO-LMO}$. The values of activation energy for hopping of all involved materials combinations are listed in Table 1. The combined effect of all physical interactions between the materials is reflected in this single value of the activation energy for diffusion. Considering how these values are applied in the KMCS model, a high value indicates favorable interactions, resulting in a wetting behavior, while a low value corresponds to a nonwetting behavior.

The values for $E_{LLTO-STO}$ and $E_{LLTO-LLTO}$ are similar, indicating similar favorable interactions that can be explained by their identical perovskite crystal structure. The value for $E_{LMO-STO}$ is significantly lower, indicating reduced wetting behavior for a spinel layer on a perovskite surface. Note that by using these values, the (non)wettability is only implicitly added to the model, which successfully reproduced the wettability for both LLTO and LMO phases on STO surfaces, as shown in Figure 2c,d, respectively. Due the Volmer−Weber growth nature of (100)-oriented LMO,[23] $E_{LMO-LMO}$ and $E_{LLTO-LMO}$ could not be obtained directly and are assumed to be equal to $E_{LLTO-LLTO}$ and $E_{LMO-STO}$, respectively, since similar interactions are expected. The obtained activation energies are used in the KMC simulation to model the VAN formation at different growth temperatures.

Figure 3 shows the KMC simulations for the VAN surface after 300 pulses of nanocomposite growth at a 20 Hz deposition rate in the temperature range 700−900 °C. The KMCS results are in good agreement with the variation in VAN formation in the experiments as shown by the AFM images in Figure 3. The LMO and LLTO components phase-separate into well-defined and evenly spaced nanostructures. The KMCS model does not incorporate anisotropic interaction energies to reflect different crystal facets and disregards the thermodynamic processes for energy minimization at the interfaces between the different material phases, that is, the nanopillars and matrix. The two components show some intermixing because the interaction energies are relatively close, while increasing the difference between these values will lead to stronger phase separation.[27] However, the simulated vertical nanostructures are qualitatively similar to those described in previous nanocomposite studies.[13,15,27−29]

Figure 4 shows the cross-sectional SEM analysis of the experimental VAN thin films for different deposition rates alongside the 3D view of the KMCS results with the same parameters. The formation of the LMO nanopillars within the LLTO matrix can be observed as they are connected to the underlying STO substrate and grow through the full thickness of the VAN film. The vertical pillars formed at 2 Hz exhibit a larger diameter compared to those grown at 8 Hz. However, for a deposition rate of 0.5 Hz, the LMO phase does not form vertical structures but grows in larger, three-dimensional


DOI: 10.1021/acsami.9b15025
ACS Appl. Mater. Interfaces 2019, 11, 44444−44450

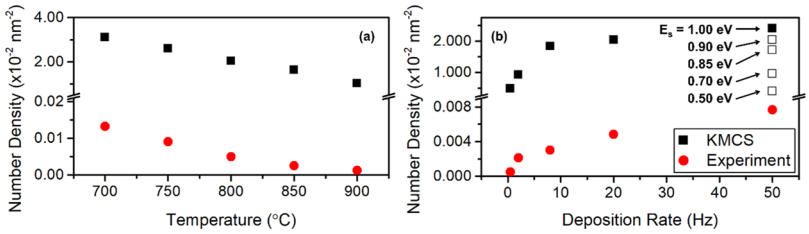


**Figure 5.** Number density comparison between KMCS (squares) and experimental results (circles) as a function of (a) different substrate temperatures for a 20 Hz deposition rate and (b) different deposition rates for a substrate temperature of 800 °C. White squares (□) in (b) represent different $E_s$ values used during simulations.

agglomerates dispersed in the LLTO matrix. Notably, many LMO structures are not well-connected to the STO substrate and instead rest on a LLTO region in many locations.

It can be clearly observed that a lower growth rate does not favor the growth of nanopillars even though particles have more time to hop over the surface to find their own species. It is expected that the formation of the pillars depends on the islands that are formed in the initial stage of growth.[13,14] The diffusion length of the two components plays a critical role in the resulting island size[27] and therefore the expected nanopillar formation. The diffusion length is given by

$$l_D = \sqrt{D\tau} \quad (1)$$

where $\tau$ is the diffusion time and $D$ is the diffusion coefficient obtained by

$$D = \nu a^2 e^{(-E_a/k_bT)} \quad (2)$$

where $\nu$ is the diffusion attempt frequency, $a$ is the characteristic jump distance, and $E_a$ is the activation energy for diffusion. At low frequencies, the long LMO diffusion length leads to the growth of a few larger islands. For higher frequencies, the diffusion length rapidly drops, resulting in the growth of many smaller islands on the surface. For such higher frequencies, the diffusion length of both LMO and LLTO species becomes comparable, and vertically aligned structures are formed. This limits the pillar diameter to about 90 nm for VAN growth at higher frequencies, in good agreement with experimental results in previous studies.[22]

A quantitative analysis was performed considering the number density of pillars over the VAN film surface. To obtain the number of pillars from the simulation results, pillar areas under 5 nm$^2$ were neglected, considering that it represents monomers on the surface. Figure 5a,b show the comparison of the number density between KMCS and experimental results, respectively, as a function of the different substrate temperatures for a 20 Hz deposition rate and the different deposition rates for a substrate temperature of 800 °C. The KMCS results show good qualitative agreement with respect to the evolution of pillar density upon changes in synthesis parameters, with a difference of a factor of 100. This difference is caused by the $E_s$ values used in the KMC simulation. For the standard simulation, $E_s$ = 1.0 eV was used, which generates good results for a low computational cost. Decreasing the value of $E_s$ (Figure 5b) allows more hops of the adatoms between consecutive pulses, yielding number density values closer to those in experiments, but with significantly longer computational times. Extrapolating KMCS number densities for different $E_s$ values from Figure 5b to the experimental number density of $7.6 \times 10^{-5}$ nm$^{-2}$ for a 50 Hz deposition rate, an $E_s$ value of 0.38 eV is calculated, resulting in an estimated increase of computational time for the KMC simulation of 2 orders of magnitude.

## CONCLUSIONS

We demonstrate the successful use of KMCS to model the growth of lithium-based vertically aligned nanocomposite films consisting of a promising LMO–LLTO cathode–electrolyte combination towards 3D solid-state batteries. For the algorithm, we applied a more realistic and low computational cost model, where a minimal number of restrictions was used for diffusion and for which the interaction energies were based on experimental RHEED measurements. The simulations, both of the individual components and of the nanocomposite VAN structures, showed good agreement with the films obtained experimentally and followed the trends for the deposition rate and temperature dependencies predicted by physical models. The simulated and experimental results show that growing at low deposition frequencies does not generate vertically aligned nanostructures, which is expected to be related to the islands formed during the initial growth stage. On the other hand, higher deposition frequencies yield comparable diffusion lengths, resulting in well-defined, but smaller, vertical nanopillars. The inverse effect is expected for variations in deposition temperature, where higher temperatures cause the formation of larger epiphyte grains. Quantitative analysis shows good agreement with respect to the evolution of nanopillar density upon changes in synthesis parameters, with a difference factor explained by the choice of energies used in the KMCS modeling to minimize the computational time. Our results demonstrate that KMCS modeling can be successfully applied to predict the nanopillar–matrix formation in lithium-based VAN films. However, to achieve optimal electrochemical functionality in the created VAN structures for energy storage, the specific crystal structure and stoichiometry have to be taken into consideration for the individual cathode and electrolyte materials, as well as for the interface formed between them.

## METHOD SECTION

The films were grown from a sintered 67% $La_{0.5}Li_{0.5}TiO_3$ + 33% $LiMn_2O_4$ (30 wt % excess Li) target at an oxygen pressure of 0.2 mbar within the temperature range 700–900 °C. A KrF excimer laser was used, operating at 248 nm, 0.5–50 Hz, and a laser energy fluence of 2.3 J cm$^{-2}$, resulting in a growth rate of ~0.15 Å/pulse. The STO substrates ($a$ = 3.905 Å)[30] were annealed in a tube oven before the deposition at 950 °C for 90 min in an oxygen flow of 150 L/h. After deposition, the films were cooled down to room temperature at an oxygen pressure of 0.2 mbar at a rate of 10 °C/min.



DOI: 10.1021/acsami.9b15025
ACS Appl. Mater. Interfaces 2019, 11, 44444–44450

For the KMCS modeling, a 3-dimensional 128 × 128 × $Z$ grid was used to represent the cubic (100) surface of STO, where $Z$ is the height. In these simulations, the PLD growth process is simplified as only deposition and diffusion of singular entities are allowed. Typically, these entities are atoms when simulating growth of metals. However, in the case of oxides, deposition and diffusion of complete unit-cell blocks are simulated, which are referred to as adatoms. The deposition of the material is simulated by instantaneously generating adatoms on randomly chosen locations on the grid. One adatom represents one unit cell of the LLTO perovskite crystal structure or 1/8th unit cell of the LMO spinel crystal structure. The number of adatoms deposited in each pulse is 1/25th of the size of the grid, based on the RHEED results for the LLTO growth rate. No desorption is allowed.

After each pulse, the deposited material can diffuse over the surface, which is modeled as the hopping of adatoms, one at a time, to available surrounding coordinates. Periodic boundary conditions were used, and hopping is only possible if a site is unoccupied and if there is a path available to it. Hopping continues until a new pulse arrives, at which moment the location of the old adatoms is fixed. The hopping rate of the adatoms is defined as $k_i = k_0\, e^{(-E_{D,i}/k_bT)}$, where $k_i$ is the hopping rate of the unit cell $i$, $k_0$ is the hop attempt frequency[13] ($k_0 = 10^{12}$ s$^{-1}$), $E_{D,i}$ is the activation energy for diffusion, $k_b$ is the Boltzmann constant, and $T$ is the absolute temperature. The activation energy was calculated considering the sum of the interaction energies between the adatom and all occupied neighboring positions, $E_D = E_S + \sum_{j=1}^{J} n_j \times E_j$, where $E_S$ is a static contribution[29] independent of neighboring sites, $n_j$ is the number of neighbors of type $j$, and $E_j$ is the interaction energy of the adatom with this neighbor. Only interactions between face-sharing adatoms are considered, and long-range interactions are ignored. Hopping can occur both in the 6 cubic and 12 diagonal directions. For diagonal hops (step-down or step-up), the Ehrlich−Schwoebel barrier ($E_{ES}$) is present due to the decreased coordination between a surface diffusing adatom and the substrate. An $E_{ES}$ value of 0.15 eV was used, in good agreement with previous studies for various materials systems.[31−33]

To perform a hopping event, a random number, $r$ ($0 < r < 1$), is generated, and the adatom with a hopping probability closer to $r{\cdot}K$ is chosen to hop, where $K$ is the cumulative sum of the hopping probabilities. Adatoms with a higher hopping rate have a higher probability of being chosen. After an adatom is selected, the $E_{ES}$ barrier determines the probability of diagonal movement. After each hop, the location of the adatoms in the ($X$, $Y$, $Z$) matrix is updated, and the hopping rates that may have changed and a new adatom is selected. The time of the simulation is updated after each hop using $\Delta t = -\log(r)/K$.[34] Once a simulation time equal to $1/f$ has passed, where $f$ is the deposition frequency, a new pulse of the material arrives, and the simulation steps begin anew.

## AUTHOR INFORMATION


### Corresponding Author

*E-mail: m.huijben@utwente.nl.

### ORCID

Mark Huijben: 0000-0001-8175-6958


### Author Contributions

The manuscript was written through contributions of all authors. All authors have given approval to the final version of the manuscript.


### Funding

Financial support by the Netherlands Organization for Scientific Research (NWO) under the VIDI grant no. 13456.


### Notes

The authors declare no competing financial interest.


## ACKNOWLEDGMENTS

D.M.C., T.A.H., D.P.S., and M.H. acknowledge support from the Netherlands Organization for Scientific Research (NWO) under VIDI grant no. 13456.


## REFERENCES


(1) Thostenson, E.; Li, C.; Chou, T. Nanocomposites in Context. *Compos. Sci. Technol.* **2005**, *65*, 491−516.

(2) Palmero, P. Structural Ceramic Nanocomposites: A Review of Properties and Powders' Synthesis Methods. *Nanomaterials* **2015**, *5*, 656−696.

(3) Stuart, M. A. C.; Huck, W. T. S.; Genzer, J.; Müller, M.; Ober, C.; Stamm, M.; Sukhorukov, G. B.; Szleifer, I.; Tsukruk, V. V.; Urban, M.; Winnik, F.; Zauscher, S.; Luzinov, I.; Minko, S. Emerging Applications of Stimuli-Responsive Polymer Materials. *Nat. Mater.* **2010**, *9*, 101−113.

(4) Zhang, W.; Ramesh, R.; MacManus-Driscoll, J. L.; Wang, H. Multifunctional, Self-Assembled Oxide Nanocomposite Thin Films and Devices. *MRS Bull.* **2015**, *40*, 736−745.

(5) Huang, J.; MacManus-Driscoll, J. L.; Wang, H. New Epitaxy Paradigm in Epitaxial Self-Assembled Oxide Vertically Aligned Nanocomposite Thin Films. *J. Mater. Res.* **2017**, *32*, 4054−4066.

(6) Zheng, H.; Wang, J.; Lofland, S. E.; Ma, Z.; Mohaddes-Ardabili, L.; Zhao, T.; Salamanca-Riba, L.; Shinde, S. R.; Ogale, S. B.; Bai, F.; Viehland, D.; Jia, Y.; Schlom, D. G.; Wuttig, M.; Roytburd, A.; Ramesh, R. Multiferroic BaTiO3-CoFe2O4 Nanostructures. *Science* **2004**, *303*, 661−663.

(7) Harrington, S. A.; Zhai, J.; Denev, S.; Gopalan, V.; Wang, H.; Bi, Z.; Redfern, S. A. T.; Baek, S.-H.; Bark, C. W.; Eom, C.-B.; Jia, Q.; Vickers, M. E.; MacManus-Driscoll, J. L. Thick Lead-Free Ferroelectric Films with High Curie Temperatures through Nanocomposite-Induced Strain. *Nat. Nanotechnol.* **2011**, *6*, 491−495.

(8) Wang, Z.; Li, Y.; Viswan, R.; Hu, B.; Harris, V. G.; Li, J.; Viehland, D. Engineered Magnetic Shape Anisotropy in BiFeO3-CoFe2O4 Self-Assembled Thin Films. *ACS Nano* **2013**, *7*, 3447−3456.

(9) Chen, A.; Bi, Z.; Tsai, C. F.; Lee, J.; Su, Q.; Zhang, X.; Jia, Q.; MacManus-Driscoll, J. L.; Wang, H. Tunable Low-Field Magnetoresistance in (La0.7Sr 0.3MnO3)0.5:(ZnO)0.5 Self-Assembled Vertically Aligned Nanocomposite Thin Films. *Adv. Funct. Mater.* **2011**, *21*, 2423−2429.

(10) Hsieh, Y. H.; Liou, J. M.; Huang, B. C.; Liang, C. W.; He, Q.; Zhan, Q.; Chiu, Y. P.; Chen, Y. C.; Chu, Y. H. Local Conduction at the BiFeO3-CoFe2O4 Tubular Oxide Interface. *Adv Mater Weinheim* **2012**, *24*, 4564−4568.

(11) Lee, O.; Harrington, S. A.; Kursumovic, A.; Defay, E.; Wang, H.; Bi, Z.; Tsai, C. F.; Yan, L.; Jia, Q.; MacManus-Driscoll, J. L. Extremely high tunability and low loss in nanoscaffold ferroelectric films. *Nano Lett* **2012**, *12*, 4311−4317.

(12) MacManus-Driscoll, J. L.; Suwardi, A.; Wang, H. Composite Epitaxial Thin Films: A New Platform for Tuning, Probing, and Exploiting Mesoscale Oxides. *MRS Bull.* **2015**, *40*, 933−942.

(13) Mouton, I.; Talbot, E.; Pareige, C.; Lardé, R.; Blavette, D. The Early Stage of Formation of Self-Organized Nanocolumns in Thin Films: Monte Carlo Simulations versus Atomic-Scale Observations in Ge-Mn. *J. Appl. Phys.* **2014**, *115*, 053515.




DOI: 10.1021/acsami.9b15025
ACS Appl. Mater. Interfaces 2019, 11, 44444−44450

(14) Ichino, Y.; Yoshida, Y.; Miura, S. Three-Dimensional Monte Carlo Simulation of Nanorod Self-Organization in REBa2Cu3Oy Thin Films Grown by Vapor Phase Epitaxy. *Jpn. J. Appl. Phys.* **2017**, *56*, 015601.
(15) Ichino, Y.; Tsuruta, A.; Miura, S.; Yoshida, Y.; Yoshizumi, M.; Izumi, T. Determinant for Self-Organization of BaMO3 Nanorods Included in Vapor-Phase-Grown REBa2Cu3Oy Films. *IEEE Trans. Appl. Supercond.* **2015**, *25*, 6995944.
(16) Hennes, M.; Schuler, V.; Weng, X.; Buchwald, J.; Demaille, D.; Zheng, Y.; Vidal, F. Growth of vertically aligned nanowires in metal-oxide nanocomposites: kinetic Monte-Carlo modeling versus experiments. *Nanoscale* **2018**, *10*, 7666−7675.
(17) Otomo, J.; Kurokawa, R.; Takahashi, H.; Nagamoto, H. Kinetic process of phase separation in Co-$SiO_2$ thin films and preparation of mesoporous $SiO_2$ thin films with mesopore channels aligned perpendicularly to substrate surfaces. *Vacuum* **2007**, *81*, 1003−1011.
(18) Long, J. W.; Dunn, B.; Rolison, D. R.; White, H. S. Three-Dimensional Battery Architectures. *Chem. Rev.* **2004**, *104*, 4463−4492.
(19) Oudenhoven, J. F. M.; Baggetto, L.; Notten, P. H. L. All-Solid-State Lithium-Ion Microbatteries: A Review of Various Three-Dimensional Concepts. *Adv. Energy Mater.* **2011**, *1*, 10−33.
(20) Thackeray, M. M. Manganese Oxides for Lithium Batteries. *Prog. Solid State Chem.* **1997**, *25*, 1−71.
(21) Stramare, S.; Thangadurai, V.; Weppner, W. Lithium Lanthanum Titanates: A Review. *Chem. Mater.* **2003**, *15*, 3974−3990.
(22) Zheng, H.; Straub, F.; Zhan, Q.; Yang, P.-L.; Hsieh, W.-K.; Zavaliche, F.; Chu, Y.-H.; Dahmen, U.; Ramesh, R. Self-Assembled Growth of BiFeO3-CoFe2O4 Nanostructures. *Adv. Mater.* **2006**, *18*, 2747−2752.
(23) Hendriks, R.; Cunha, D. M.; Singh, D. P.; Huijben, M. Enhanced Lithium Transport by Control of Crystal Orientation in Spinel LiMn2O4 Thin Film Cathodes. *ACS Appl. Energy Mater.* **2018**, *1*, 7046−7051.
(24) Ohta, H.; Mizoguchi, T.; Aoki, N.; Yamamoto, T.; Sabarudin, A.; Umemura, T. Lithium-Ion Conducting La2/3xLi3xTiO3 Solid Electrolyte Thin Films with Stepped and Terraced Surfaces. *Appl. Phys. Lett.* **2012**, *100*, 173107.
(25) Blank, D. H. A.; Rijnders, G. J. H. M.; Koster, G.; Rogalla, H. A New Approach in Layer-by-Layer Growth of Oxide Materials by Pulsed Laser Deposition. *J. Electroceram.* **2000**, *4*, 311−318.
(26) Rijnders, G.; Blank, D. H. A.; Choi, J.; Eom, C.-B. Enhanced Surface Diffusion through Termination Conversion during Epitaxial SrRuO3 Growth. *Appl. Phys. Lett.* **2004**, *84*, 505−507.
(27) Zheng, S.; Zhu, W.; Gao, Y. F.; Stocks, G. M.; Zhang, Z. Kinetic Monte Carlo Simulations of Nanocolumn Formation in Two-Component Epitaxial Growth. *Appl. Phys. Lett.* **2010**, *96*, 071913.
(28) Walter, J.-C.; Barkema, G. T. An Introduction to Monte Carlo Methods. *Phys. A* **2015**, *418*, 78−87.
(29) Lam, P.-M.; Liu, S. J.; Woo, C. H. Monte Carlo Simulation of Pulsed Laser Deposition. *Phys. Rev. B: Condens. Matter Mater. Phys.* **2002**, *66*, 045408.
(30) Herger, R.; Willmott, P. R.; Bunk, O.; Schlepütz, C. M.; Patterson, B. D.; Delley, B.; Shneerson, V. L.; Lyman, P. F.; Saldin, D. K. Surface Structure of SrTiO3 (001). *Phys. Rev. B: Condens. Matter Mater. Phys.* **2007**, *76*, 195435.
(31) Ehrlich, G. Atomic Displacements in One- and Two-Dimensional Diffusion. *J. Chem. Phys.* **1966**, *44*, 1050−1055.
(32) Schwoebel, R. L.; Shipsey, E. J. Step Motion on Crystal Surfaces. *J. Appl. Phys.* **1966**, *37*, 3682−3686.
(33) Meyer, J. A.; Vrijmoeth, J.; van der Vegt, H. A.; Vlieg, E.; Behm, R. J. Importance of the Additional Step-Edge Barrier in Determining Film Morphology during Epitaxial Growth. *Phys. Rev. B: Condens. Matter Mater. Phys.* **1995**, *51*, 14790.
(34) Maksym, P. A. Fast Monte Carlo Simulation of MBE Growth. *Semicond. Sci. Technol.* **1988**, *3*, 594−596.


DOI: 10.1021/acsami.9b15025
*ACS Appl. Mater. Interfaces* 2019, 11, 44444−44450